Journal of Asian Earth Sciences 263 (2024) 106035

Contents lists available at ScienceDirect

Journal of Asian Earth Sciences

journal homepage: www.elsevier.com/locate/jseaes

A flat lithosphere-asthenosphere boundary (~60 km depth) in central Eastern China: Implications for lithospheric destruction and evolution

Xinfu Li [a,b,*], Xiaobo He [c], Shuo Xu [b], Hongyi Li [a,b], Guoming Jiang [a,b]

[a] Key Laboratory of Intraplate Volcanoes and Earthquakes (China University of Geosciences, Beijing), Ministry of Education, Beijing 100083, China
[b] School of Geophysics and Information Technology, China University of Geosciences, Beijing 100083, China
[c] Marine Science and Technology College, Zhejiang Ocean University, Zhoushan 316022, Zhejiang, China

ARTICLE INFO

Keywords:
Sp receiver functions
Central Eastern China
Lithosphere-asthenosphere boundary
Lithospheric thinning

ABSTRACT

Detailed knowledge of the lithospheric thickness is important for understanding the tectonic evolution in central Eastern China, characterized by ore deposits in the Middle-Lower Yangtze Metallogenic Belt (MLYMB). We realize this goal by applying the common conversion point (CCP) stacking to Sp receiver functions (SRF) computed from 234 broadband seismic stations in central Eastern China. Distinct negative signals are identified below the Moho in all the CCP stacking profiles, which we interpret as the S-to-P conversions from the lithosphere-asthenosphere boundary (LAB). The imaged LAB is as shallow as ~60 km with a standard deviation of ~5 km in the whole region, in contrast to the typical cratonic lithosphere root down to 200 km depth or more, indicating the widespread lithospheric thinning in the study region. Such a flat LAB indicates that the regional lithosphere has been destructed uniformly, shedding light on its destructive mechanism, which we attribute to lithospheric delamination along a mid-lithospheric discontinuity (MLD). Compared to the MLD (~80–100 km) observed in the western North China Craton, our observations suggest that the destructed lithosphere probably has been further stretched due to slab rollback and trench retreat. In contrast, lithospheric cooling-induced accretion plays a minor role in the lithospheric evolution after destruction.

1. Introduction

Central Eastern China mainly consists of the Eastern North China Craton (NCC) in the north and the South China Block (SCB) in the south (Zheng et al., 2013 ; Li et al., 2018) (Fig. 1). The NCC, mainly made up of the Western Block and the Eastern Block, was formed by the amalgamation along the Trans-North China Orogen in the Paleoproterozoic at ~1.8 Ga (Zhai and Santosh, 2011) and consists of a thick Mesoproterozoic to Neoproterozoic and Paleozoic basement (Wu et al., 2003a,b). The SCB is divided into the Yangtze Craton (YC) in the northwest and the Cathaysia Block (CaB) in the southeast by a SW-NE trending suture. Especially in the northeastern part of SCB, the Jiangnan collisional orogen that welded together the Yangtze and the Cathaysia blocks, to the North and South, respectively is well acknowledged by the presence of ophiolites, subduction complexes, and HP rocks (e.g. Shu et al.,1994, 2006; Li et al., 2009; Faure et al., 2016, 2017). The closure of a paleo-Tethys Ocean, induced by the northward subduction of the YC beneath the NCC at ~245–210 Ma (Hacker et al., 2006; Zhang et al., 2009), caused the collision of the NCC and SCB during the Triassic. This collision finally generated the Qinling-Dabie-Sulu orogenic belt-the most famous high and ultrahigh-pressure (HP and UHP) metamorphic zone in the world (Meng and Zhang, 2000; Hacker et al., 2006; Zhang et al., 2009). The Tancheng-Lujiang Fault (TLF) divided the Dabie-Sulu orogenic belt into the southwestern Dabie and northeastern Sulu segments owing to the sinistral strike-slip activities in the Mesozoic (Wang, 2006). The Triassic subduction and collision-tectonics produced intense deformation, magmatism, and metamorphism across the entire SCB (Chu et al., 2020).

Numerous investigations into the details of regional geological, geochemical, and petrological characteristics in Eastern China have been conducted (e.g., Ling et al., 2009; Mao et al., 2011; Li et al., 2013b; Zheng et al., 2003; Zhou and Li, 2000). They have significantly improved our understanding of the regional tectonic evolution. The N-S compression caused by the early Paleozoic collision between the NCC and the SCB was followed by a series of destructions of the lithosphere during the Jurassic and the Cretaceous. This led to significant lithosphere thinning, intensive metallogenesis, and strong magmatic activities (Li and Li, 2007; Zhu et al., 2012a,b). Accordingly, the tectonic

* Corresponding author.
E-mail address: xinfuli@cugb.edu.cn (X. Li).

https://doi.org/10.1016/j.jseaes.2024.106035
Received 18 August 2023; Received in revised form 11 January 2024; Accepted 25 January 2024
Available online 1 February 2024

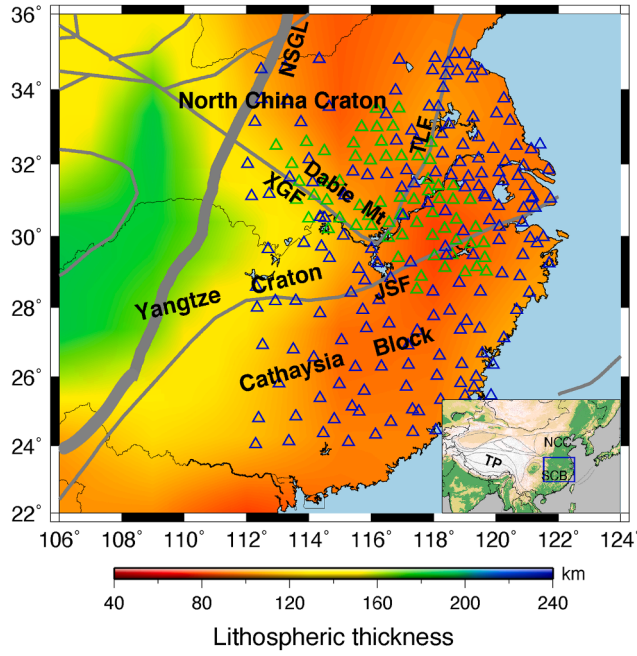

Fig. 1. Topography and major tectonic units in and around our study region. The green triangles indicate temporary stations deployed by China University of Geosciences (Beijing) (CUGB) during different periods between June 2012 and July 2016; the blue triangles are stations from China Digital Seismic Network (Data Management Centre of China National Seismic Network., Zheng et al., 2010). The thin gray lines indicate the boundaries of major tectonic units. TLF: Tancheng-Lujiang fault (Tanlu fault); XGF: Xiangfan-Guangji fault; JSF: Jiangshao fault; NSGL: North-South Gravity Lineament. The insert map in the lower right corner represents a tectonic sketch of the study and adjacent areas. TP: Tibetan Plateau; NCC: North China Craton; SCB: South China Block.

regime shifted from compression in the Early Mesozoic to extension in the Late Mesozoic (Chu et al., 2012a,b; 2019, 2020; Faure et al., 1996,2009). From the Late Mesozoic through the whole Cenozoic, extension is thought to play a dominant role in the deformation of the lithosphere in Eastern China (Yin, 2010). Regrettably, a complete discussion on how the lithosphere responded to the transition of the tectonic regime and the continued Cenozoic extension remains pending. Moreover, direct seismological observations of the nature of the lithosphere, especially regarding the lithosphere thickness, are limited but important in revealing the lithosphere evolution.

Much seismological research in Eastern China has been conducted in the past two decades. Still, most of these studies focus on the Eastern NCC, leaving the NCC-SCB transition area undetected. (e.g., Xu et al., 2001; Zhao et al., 2007; Chang et al., 2009; Chen, 2010; Ouyang et al., 2014; Zheng et al., 2014; Lü et al., 2015). In addition, the mechanisms accounting for lithosphere destruction are also controversial. Different geodynamic models have been proposed to explain the widespread magmatic activities and intensive metallogenesis that occurred in Eastern China, e.g., the subduction of the Paleo-Pacific oceanic plate underneath mainland China (Zhou and Li, 2000; Zhou et al., 2006; Sun et al., 2012; Wang et al., 2017) mainly involving either flat-slab subduction (Li et al., 2013b; Li and Li, 2007) or the mid-ocean ridge subduction (Ling et al., 2009; Sun et al., 2010), and delamination of lower continental crust of overriding lithosphere (Xu et al., 2002). These models generally consider lithospheric thinning to be the primary factor affecting Late Mesozoic magmatism. The underlying mechanism responsible for the regional lithospheric thinning is being investigated. Therefore, this study aims to provide seismological observations on deep crustal and uppermost mantle structures to address these competing destruction models and gain a better understanding of the tectonic evolution of Eastern China.

Receiver function imaging has become a useful and widely used tool in studies of the crust and upper mantle beneath stable continents and tectonically active margins (Zhu and Kanamori, 2000; Ainsworth et al., 2014). In this paper, we employ Sp receiver function imaging to characterize central Eastern China's lithosphere-asthenosphere boundary (LAB) with seismic data collected from unprecedentedly densely-spaced broadband arrays. We discuss the possible lithosphere destructive mechanism and regional lithospheric evolution history based on the revolved LAB pattern.

2. Methods and data analysis

Receiver function imaging has been widely used to characterize mantle discontinuities (Zhu and Kanamori, 2000; Ainsworth et al., 2014). Here we apply the Sp receiver function method to detect the signals from the LAB (e.g., Kumar et al., 2005a,b, 2012) in central Eastern China, which avoids interference by the crustal multiples that the P-wave receiver functions often encounter (Farra and Vinnik, 2000; Kumar et al., 2005a,b; Rychert et al., 2007; Shen, 2011; Yuan et al., 2006). A detailed description of the SRF method can refer to a decent work by Yuan et al. (2006).

In this study, we analyzed seismic waveform data from a portable network operated by China University of Geosciences (Beijing) (CUGB) from May 2012 to July 2016, which consisted of the deployment of 64 broadband seismometers with stations spacing ~50 km (Li et al., 2015), along with data from China Digital Seismic Networks consisting of 170 broadband seismic stations which operated from January to December of 2016 (Data Management Centre of China National Seismic Network, 2007, Zheng et al., 2010) (Fig. 1). The combined datasets yield an unprecedentedly dense coverage of seismic data in the studied area.

Our SRF dataset consists of 124 teleseismic events with S-phase from 55 to 100° epicentral distances with a magnitude greater than 5.5 (Fig. 2). All the waveforms were carefully visually inspected for clear S-wave arrivals in the appropriate time window. The traces were windowed and tapered to extract 150 s before and 50 s after the direct S arrivals, and then bandpass filtered with corner frequencies at 0.01 and 0.3 Hz. This time is long enough to include all the information from crust depths and Sp phases through LAB. Data were downsampled to 10 samples per second. The traces were then rotated from the geographic coordinate system (Z-N-E) to the local P-SV-SH ray-based coordinate system (Vinnik, 1977; Kind et al., 1995; Dahl-Jensen et al., 2003). Theoretical arrival times were then calculated by using the IASP91 model (Kennett and Engdahl, 1991), and relative travel-time residuals were then measured. The waveforms were aligned along the S-phase arrival for each event using a multichannel cross-correlation algorithm (VanDecar and Crossen, 1990). Only the waveforms with residuals smaller than 3 s were kept for receiver function analysis. Fig. 3 shows the relative travel-time residuals of stations HF22 and CZ09 with respect to different events. Finally, a time-domain iterative deconvolution algorithm was used to compute SRFs (Ligorría and Ammon, 1999). All the traces were time-reversed, and amplitudes were polarity-reversed so that positive amplitudes indicate a velocity increase with depth, and negative amplitudes indicate a velocity decrease with depth. After deconvolution, the data were reinspected, and anomalous traces were deleted. To suppress noise and enhance spatial consistency of Sp conversion phase from the LAB, we first continuously performed a move-out correction of raw SRFs in the time-domain with a constant ray parameter of 0.0573 s/km (corresponding to slowness of 6.4 s/° or an epicentral distance of 67°) by using the iasp91 1D velocity model (Kennett and Engdahl, 1991), and then conducted common conversion point (CCP) stacking (Dueker and Sheehan, 1997; Kosarev et al., 1999; Zhu, 2000,2002) and migrated it into the depth domain referring to the IASP91 model.

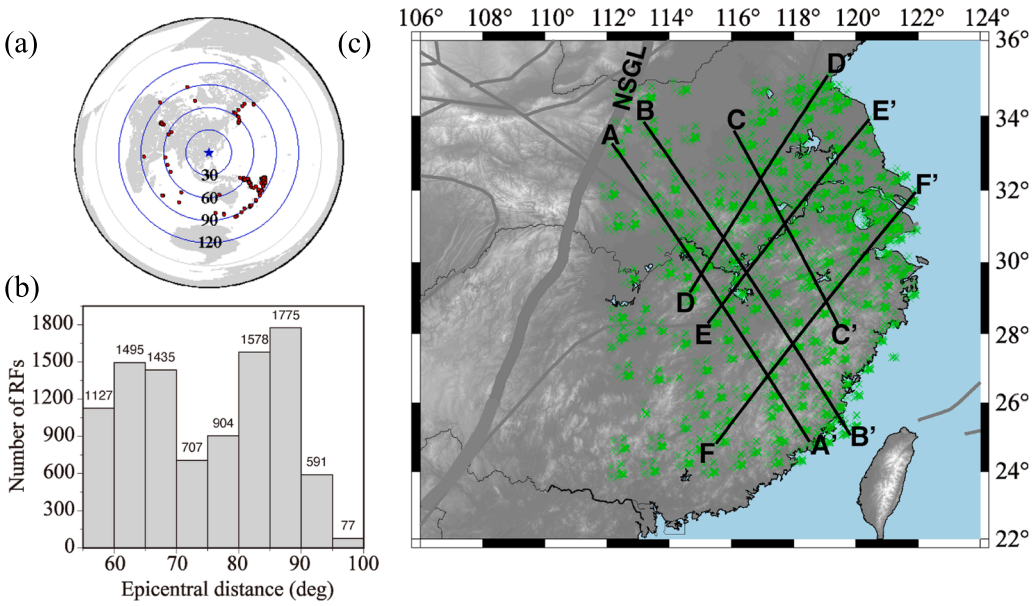

Fig. 2. (a) Distribution of the teleseismic events (red dots) used to calculate SRFs. The blue pentagram is the location of the center of the study region. (b) Statistical histogram of the epicentral distance of events. Most events are located at the epicentral distance of 55–95 degrees, while a small number of events are distributed at the epicentral distance of 95–100 degrees. (c) The green crosses represent the SRF piercing points at a depth of 60 km. The black solid lines represent profiles (AA', BB,' CC,' DD,' EE', and FF') along which the LAB images were constructed in this study (Fig. 5) using SRFs recorded at broadband seismic stations.

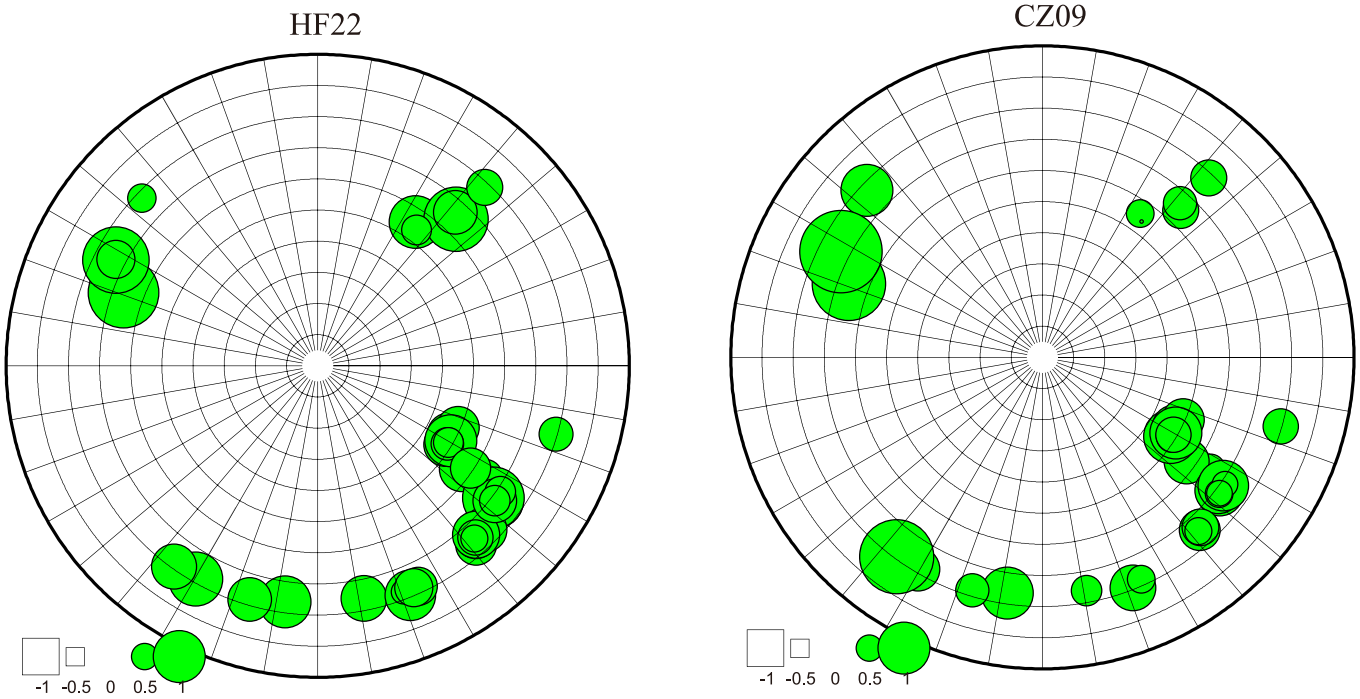

Fig. 3. Relative S-wave travel-time residuals at station HF22 and CZ09 for all the recording events concerning the IASP91 model. The square in the bottom left of each subfigure represents the negative travel-time residual, and the solid circle represents the positive travel-time residual. Different sizes represent different relative travel-time residuals.

3. Results

Fig. 4 shows Sp receiver functions of all the stations along each profile shown in Fig. 2. The station names are listed on the left. The SRFs were deconvolved with a Gaussian parameter of 1.0, and the dashed rectangles marked the approximate arrival times of the LAB phases. Fig. 5 shows the resulting images along the six profiles AA', BB', CC', DD', EE' and FF' marked in Fig. 2. The clear negative phases (blue color) appeared around ~55–65 km depth in the CCP stacked sections of the SRFs which we interpret as LAB. The LAB appears as a relatively flat surface at an average depth of ~60 km with a standard deviation of ~5 km in this area (Fig. 6). The Moho (positive phases indicated as red color around ~30 km) is continuously visible.

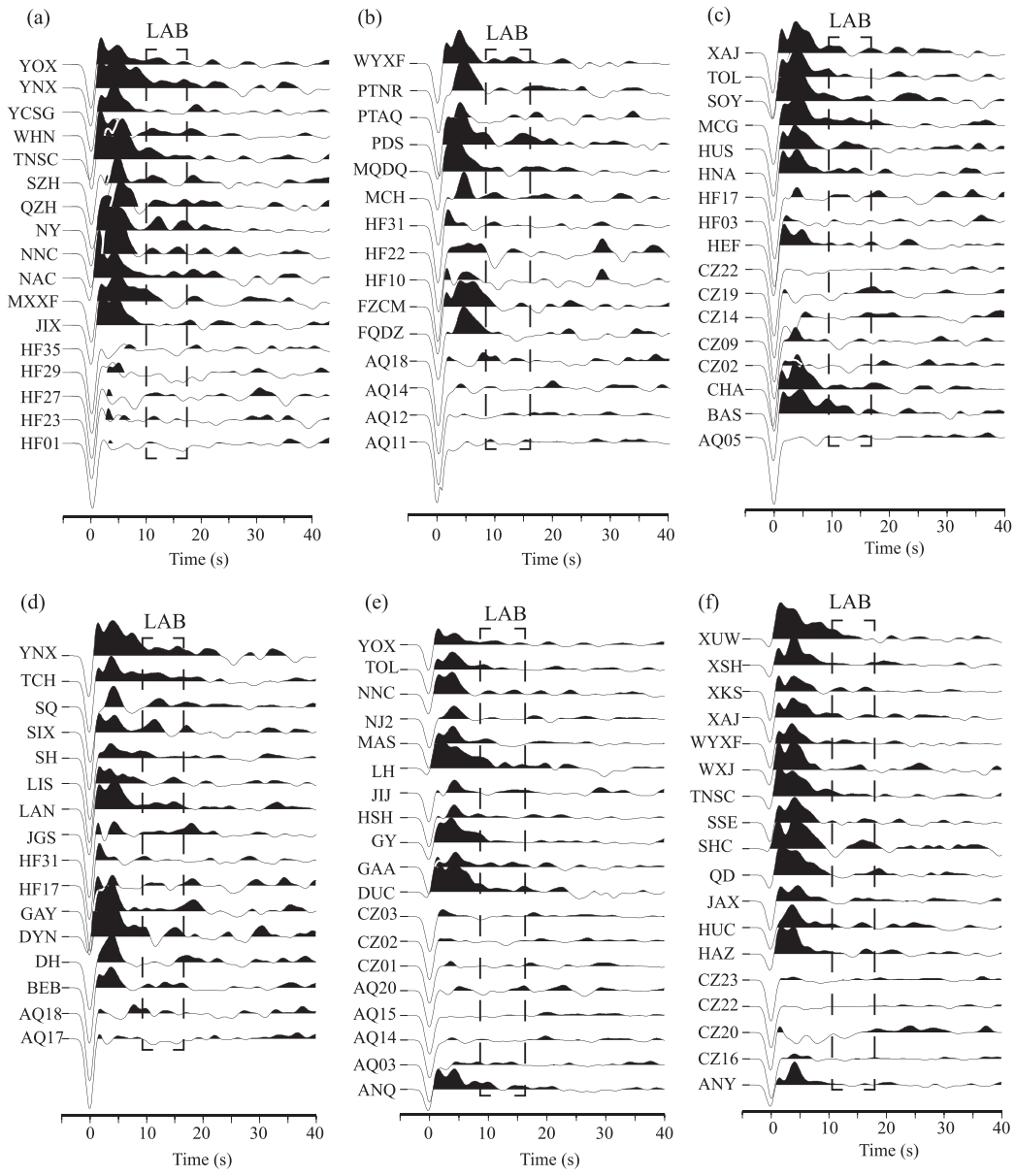

Fig. 4. S-wave receiver functions of all the stations along each profile shown in Fig. 2. The station names are listed on the left. The SRFs were deconvolved with a Gaussian parameter of 1.0, and the dashed rectangles mark the approximate arrival times of the LAB phases.

4. Discussions

4.1. Comparisons with a variety of geophysical properties

Our RFs images show that central-eastern China is characterized by an extremely thin lithosphere (~60 km) (Fig. 6b), in contrast to the ~150-180 km thick lithosphere in the west (Fig. 6a). More importantly, the thinned lithosphere appears to distribute in central-eastern China uniformly, i.e., no strong variations in the lithosphere thickness are observed, suggesting a similar destruction process that probably occurred coevally. Note that the variations in LAB depth are still observed to some extent. Such small perturbations exhibited in the result can be attributed to (1) lateral variations in velocity heterogeneities because a simple one-dimensional IASP91 model was considered when time-depth conversions were conducted and (2) limited vertical resolution when low-frequency teleseismic waves were used. Compared to the one-dimensional model, a three-dimensional structural model may lead to a variation of 5 km or less, depending on the complexity of the regional velocity model. The lateral resolution of SRFs is mainly determined by the Fresnel zone of LAB phases, which is a function of the dominant frequency of S waves and velocity at the LAB. It is estimated to be ~20 km. The SRFs are not ideal for resolving the sharpness of LAB due to the low frequencies of S waves. The depth resolution is estimated to be ~15 km. The resolved LAB depth of 60 ± 5 km in this region can be attributed to a uniform LAB, although several factors could introduce perturbation to the LAB depths.

Several seismic investigations have revealed that central-eastern China has experienced widespread lithospheric thinning (e.g., Chen et al., 2009; Wang et al., 2017; Zheng et al., 2014) with varying lithospheric thickness given by different seismological measurements (e.g., An and Shi, 2006; Shan et al., 2014, 2020; Zhang et al., 2018). Specifically, An and Shi (2006) presented a lithospheric thickness distribution of continental China based on a 3D shear-wave velocity structure. They showed a thin lithosphere of ~80 km in both the Cathaysia block and eastern Yangtze craton and a thick lithosphere of ~180 km in west China (Fig. 6a), showing a general lithospheric thinning trend from west to east. Using a wave equation-based migration technique of the S-receiver function, Zhang et al. (2019) investigated the lithospheric structure of

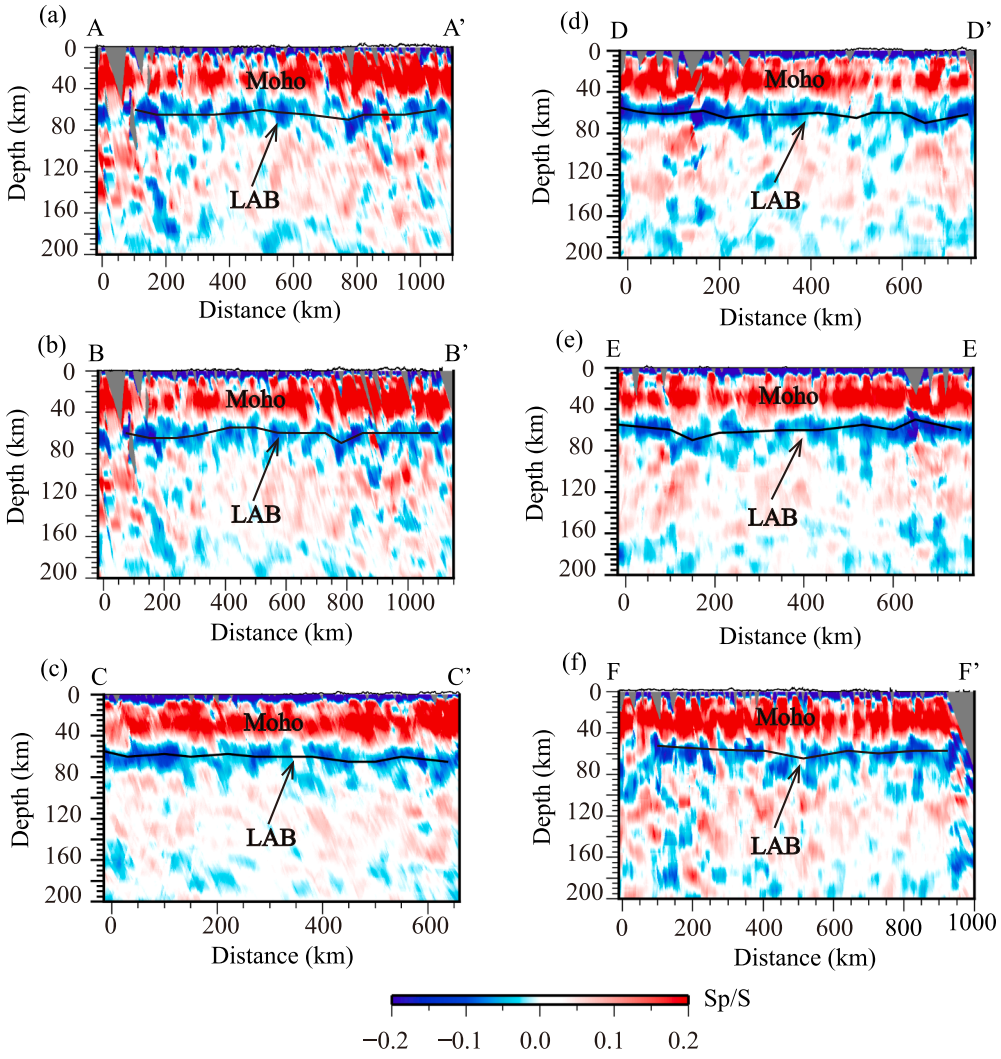

Fig. 5. SRF CCP stacked images along profiles AA', BB', CC', DD', EE' and FF' shown in Fig. 1 as solid black lines. Positive amplitudes indicate an increase in velocity with depth; negative amplitudes reflect a decrease in velocity with depth. The discontinuities labeled "Moho" is the Moho. The discontinuities labeled "LAB" is interpreted to be a transitional zone between the lithosphere and asthenosphere that has a layered character.

the lower Yangtze craton and its adjacent regions. Their results show that the LAB depth is ~84 km. Zhou et al. (2012) inferred that the lithospheric thickness in the Cathaysia block is approximately 60–70 km based on ambient noise tomography. The results from the receiver function analyses indicate a lithospheric thickness of ~60 km in the central and northern Cathaysia block (Li et al., 2013a; Zheng et al., 2014; Zhang et al., 2018). Recently, Wang et al. (2017) conducted an ambient noise tomography that includes eastern China and the marginal seas of the Chinese coast and found that both the crustal and lithospheric thickness thin progressively from NW to SE direction. In summary, based on previous observations, the lithosphere in eastern China has been thinned to 60–70 km (Liu et al., 2012). Our results generally agree with the previous measurements but show more uniform regional signatures.

In addition, other geophysical properties such as Sn velocity (Pei et al., 2007), effective elastic thickness (Te) (Deng et al., 2014), surface heat flow (Jiang et al., 2019), and Curie-point depth (Xiong et al., 2016) are employed for comparisons (Fig. 7). It is clear to see (1) the agreement between various properties and (2) that the areas with thinned lithosphere exhibit low Sn velocity, small Te, elevated heat flow, and shallow Curie-point depth. All the parameters can be explained as a result of lithosphere destruction that leads to thermal perturbations in the uppermost mantle. That is, thermal anomaly lowers the Sn velocity, weakens the lithosphere, increases the heat flow in the surface, and elevates the Cure-point depth. All the signatures point to the lithosphere in central-eastern China, which must have been subjected to extensive destruction. It is also worth mentioning that each physical property shows spatial variations to some extent (Fig. 7(a-d)). The variations can be attributed to additional thermal contributions from radiogenic heat, which are heterogeneously distributed in the continental crust (Jaupart et al., 2016). It has been well-accepted that two factors affect the heat in the lithosphere: the conduction heat dependent on the lithosphere thickness and the radiogenic heat.

4.2. *Possible cause of the lithosphere thinning*

Based on magmatic activities and numerical simulations, several mechanisms have been proposed to explain the lithosphere destruction in Eastern China (e.g., Liu et al., 2019). They can be generally classified into two regimes. The first is a bottom-up process that disturbs the lithosphere from below through thermal-chemical processes (e.g., He, 2014) or hydration-induced thinning (e.g., Liao et al., 2017; Sun et al., 2021). The second is a top-down process (i.e., the delamination model) that destroys the lithosphere through lower crust delamination (e.g., Gao et al., 1998) or mid-lithospheric discontinuity (MLD) delamination (e.g., Wang et al., 2018; Shi et al., 2020). All the processes are associated with the subduction of the Paleo-Pacific plate, very likely with a flat-slab

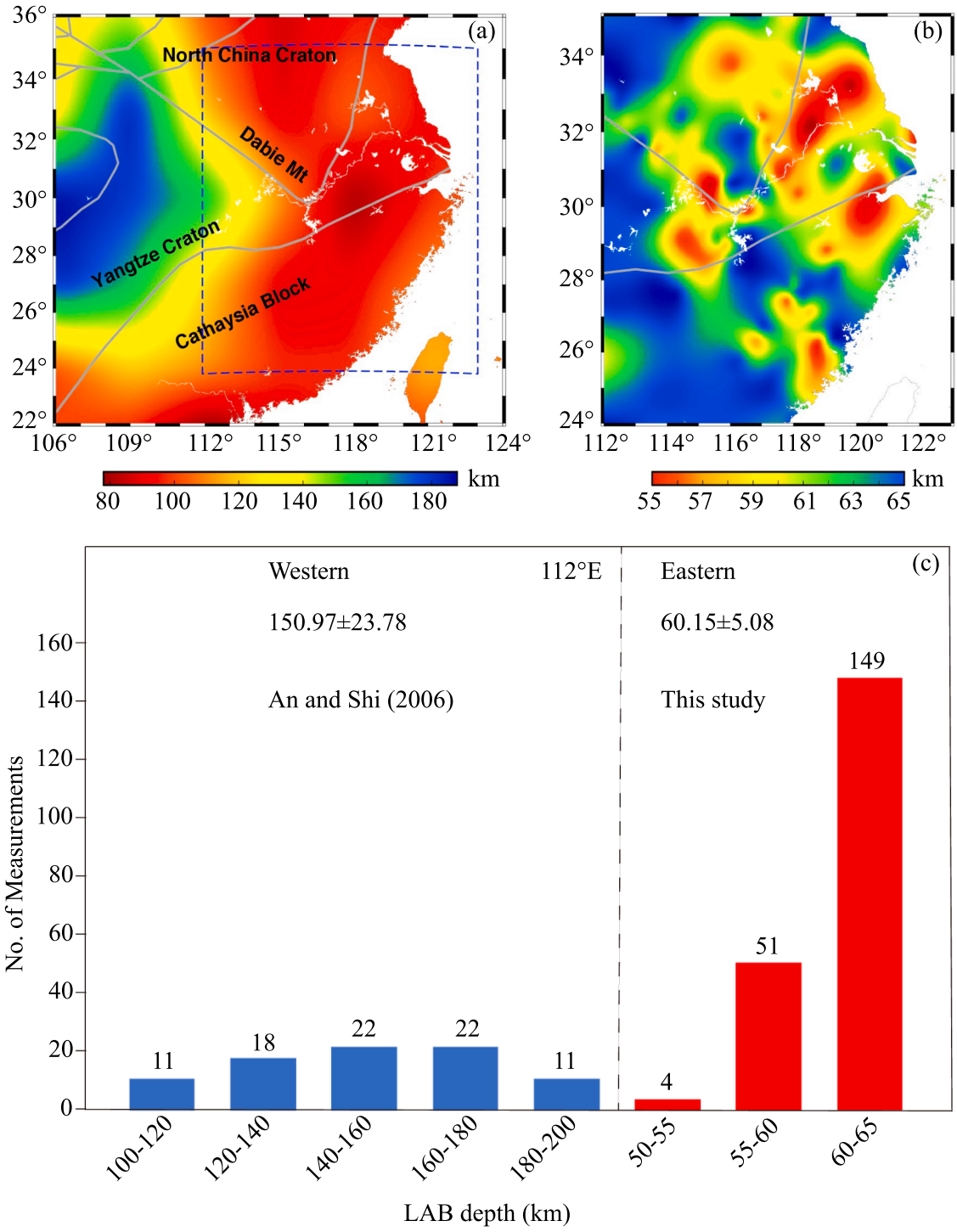

Fig. 6. (a) LAB depth variations in the studied region and surroundings given by An and Shi (2006) from a tomographic inversion result, and the blue rectangle shows our studying area. (b) LAB depth variations obtained from receiver functions analysis in this study, showing an average value of ~60 km with a standard deviation of ~5 km. (c) Histograms show the distinct lithosphere thickness between the western and eastern subregions, separated at 112°E.

scenario favored by the arrival of buoyant terrane (e.g., Li and Li, 2007), which have been evidenced by massive magmatic activities (Zheng et al., 2014; Li et al., 2018) and numerical simulations (e.g., Liu et al., 2021a,b).

Based on the seismological observations, narrowing down the mechanism that solely led to the lithospheric destruction is still challenging because the current lithosphere characteristics reflect the present-day status, not the past. Fortunately, this study captures a distinctive sign that the lithosphere was thinned uniformly. This characteristic is very important because it can help rule out the mechanisms that more often cause heterogeneous destructions (i.e., strong variations in lithosphere thickness), in which the bottom-up process and lower crust delamination can thus be excluded. It can be understood that the fluids-related and thermal-chemical processes, as well as crustal eclogization-induced densification, are more likely to occur unevenly. Therefore, the destruction model applied to central-eastern China is likely limited to MLD delamination because it can destroy the lithosphere more uniformly.

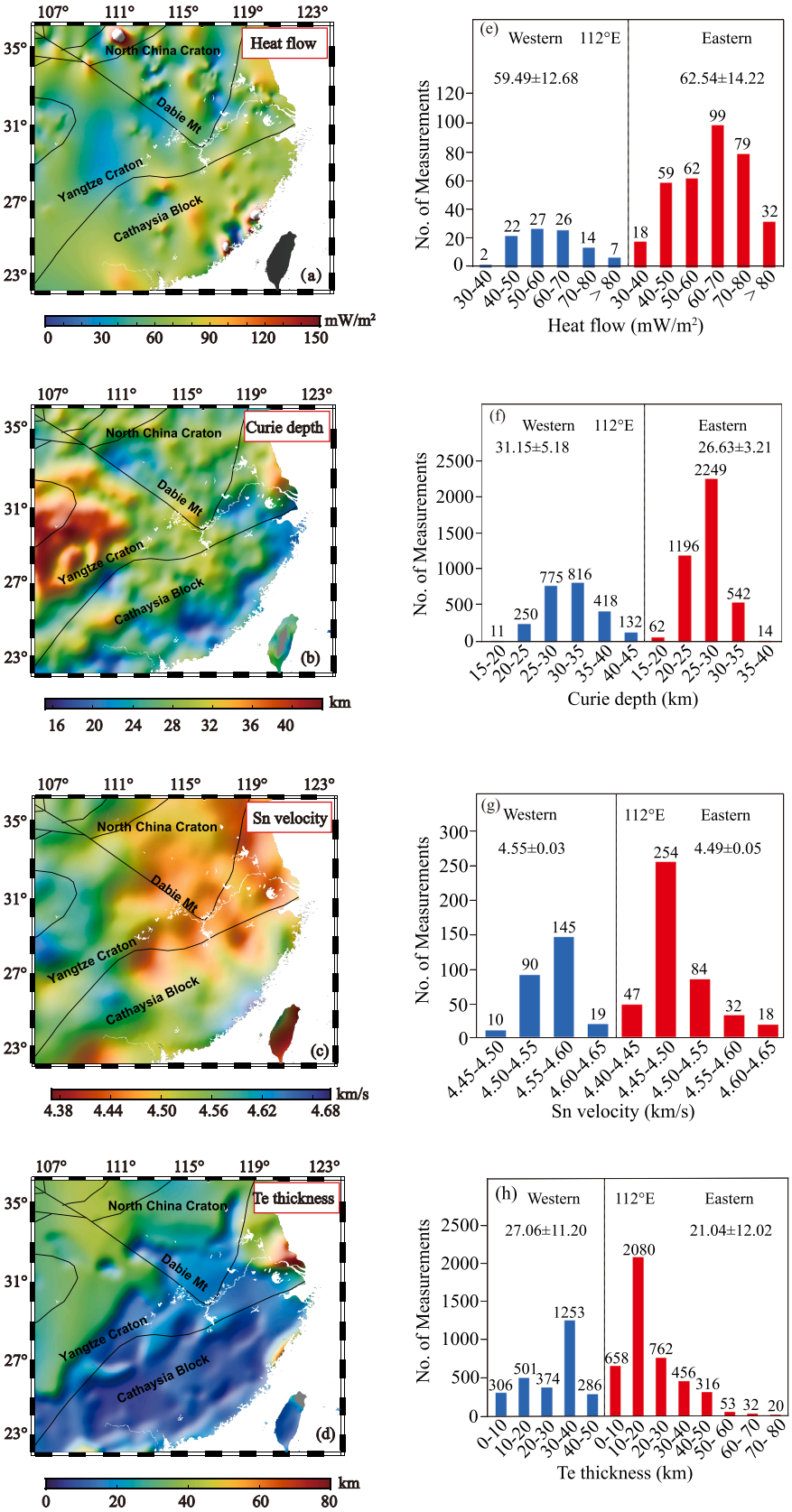

Fig. 7. (a) Heat flow distribution of Eastern China (Jiang et al., 2019). (b) Sn velocity distribution of Eastern China (Pei et al., 2007). (c) Curie-point depth of Eastern China (Xiong et al., 2016). (d) The effective elastic thickness (Te) of the lithosphere of Eastern China (Deng et al., 2014). (e-h) The corresponding histograms for the geophysical properties displayed in (a-d). For statistics, the region is divided into western and eastern subregions, separated at 112°E. Notably, western and eastern properties are distinct.

4.3. The processes leading to the ~60 km thick lithosphere

If we accept (1) the delamination process as the main cause for the loss of its lower portion of proto-lithosphere along the weak zone of MLD and (2) that the MLD existed at a depth of ~80–100 km as suggested by seismological constraints on the central and western North China Craton (Chen et al., 2014) and 78 km with a standard deviation of 13 km for Nubia/Somalia/Arabia (Liu et al., 2021a,b), an additional process is thus required to reconcile the present-day ~60 km thick and the 80–100 km MLD depths; that is, this process further stretched the destructed lithosphere to 60 km thick, which we attribute to slab rollback and trench retreat. This is in accordance with the structural geology analyses in this area that concluded that the large-scale compression and extension in the South China block was probably triggered by the rollback of the Paleo-Pacific subduction zone (Chu et al., 2012a, b, 2020). The crustal stretching started regionally since the Late Jurassic (Wei et al., 2016). In contrast, cooling-induced accretion after the destruction may play a minor role in thickening the lithosphere. The series of lithospheric modifications is illustrated in Fig. 8. This process is consistent with sedimentary records in Eastern China, showing the late Mesozoic transformation from the compressive to the extensional tectonic regime (Yu et al., 2023). Independent observations also suggest that the South China block experienced two cycles of compression-extension at 155–120 and 120–85 Ma (Chu et al., 2019). This tectonic swift is probably attributed to the Paleo-Pacific subduction angle change and lithospheric foundering of the upper plate (Chu et al., 2019). Various lines of evidence are in agreement with our lithospheric evolution model.

5. Conclusions

This study employed S-wave receiver function analysis to seismic data collected from a densely spaced network in central Eastern China. The revealed regional LAB is at a depth of ~60 km, indicating that the lithospheric mantle has been largely destroyed. Based on the uniformly thin characteristics, we attribute the destruction to lithosphere delamination along the weak MLD associated with the subduction of the paleo-Pacific plate. In contrast, the current ~60 km thick lithosphere is a competitive result between slab rollback-induced thinning and cooling-induced accretion after the MLD delamination.

CRediT authorship contribution statement

Xinfu Li: Writing – original draft, Visualization, Validation, Methodology, Investigation, Formal analysis. **Xiaobo He:** Writing – review & editing, Supervision. **Shuo Xu:** Software, Formal analysis, Data curation. **Hongyi Li:** Investigation, Data curation. **Guoming Jiang:** Investigation, Data curation.

Declaration of competing interest

The authors declare that they have no known competing financial interests or personal relationships that could have appeared to influence the work reported in this paper.

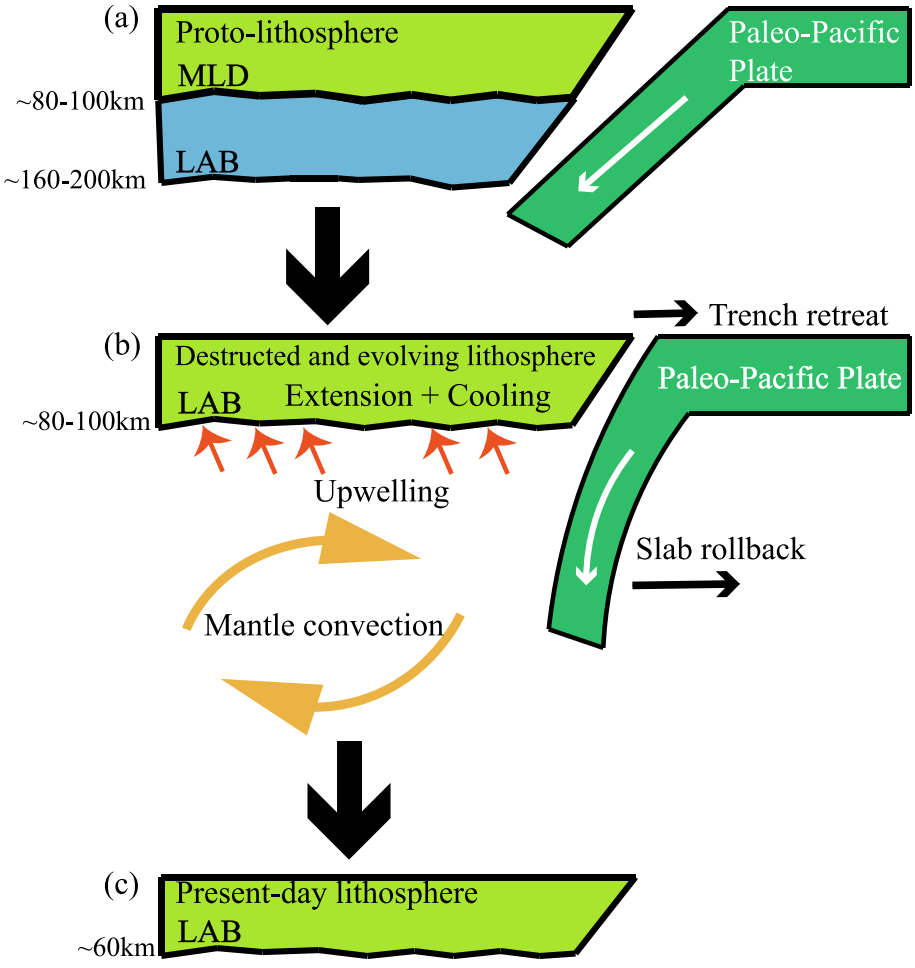

Fig. 8. Lithosphere structure and schematic model for lithospheric modification.

Data availability

The authors do not have permission to share data.

Acknowledgements

Waveform data for this study are partially provided by the Data Management Centre of China National Seismic Network at the Institute of Geophysics (SEISDMC, doi:10.11998/SeisDmc/SN), China Earthquake Networks Center and AH, FJ, HB, HE, HN, JS, JX, ZJ Seismic Networks, China Earthquake Administration. This research was co-supported by the National Natural Science Foundation of China (41474045, 42276049) and National Key Research and Development Program of China (2016YFC0600201-2). The GMT software package (Wessel and Smith, 1995) was used for making the figures. The editor Michel Faure and the two anonymous reviewers provided constructive comments and suggestions, which have improved the manuscript significantly.

References

Ainsworth, R., Jay, P., Harold, G., Dominic, E., 2014. Sp receiver function imaging of a passive margin: Transect across Texas's Gulf Coastal Plain. Earth Planet. Sci. Lett. 402, 138–147. https://doi.org/10.1016/j.epsl.2014.05.056.

An, M., Shi, Y., 2006. Lithospheric thickness of the Chinese continent. Phys. Earth Planet. in. 159, 257–266.

Chang, L., Wang, C., Ding, Z., 2009. Seismic anisotropy of upper mantle in Eastern China. Sci. China Earth Sci. 52 (6), 774–783. https://doi.org/10.1007/s11430-009-0073-4.

Chen, L., 2010. Concordant structural variations from the surface to the base of the upper mantle in the North China Craton and its tectonic implications. Lithos 120 (1–2), 96–115. https://doi.org/10.1016/j.lithos.2009.12.007.

Chen, L., Cheng, C., Wei, Z., 2009. Seismic evidence for significant lateral variations in lithospheric thickness beneath the central and western North China Craton. Earth Planet. Sci. Lett. 289, 171–183.

Chen, L., Jiang, M., Yang, J., Wei, Z., Liu, C., Ling, Y., 2014. Presence of an intralithospheric discontinuity in the central and western North China Craton: Implications for destruction of the craton. Geology 42 (3), 223–226.

Chu, Y., Faure, M., Lin, W., Wang, Q., 2012a. Early Mesozoic tectonics of the South China block: Insights from the Xuefengshan intracontinental orogen. J. Asian Earth Sci. 61, 199–220.

Chu, Y., Faure, M., Lin, W., Wang, Q., Ji, W., 2012b. Tectonics of the Middle Triassic intracontinental Xuefengshan Belt, South China: New insights from structural and chronological constraints on the basal décollement zone. Int. J. Earth Sci. 101 (8), 2125–2150.

Chu, Y., Lin, W., Faure, M., Xue, Z., Ji, W., Feng, Z., 2019. Cretaceous episodic extension in the South China Block, East Asia: Evidence from the Yuechengling Massif of central South China. Tectonics 38, 3675–3702. https://doi.org/10.1029/2019TC005516.

Chu, Y., Lin, W., Faure, M., Allen, M.B., Feng, Z., 2020. Cretaceous exhumation of the Triassic intracontinental Xuefengshan Belt: Delayed unroofing of an orogenic plateau across the South China Block? Tectonophysics 793, 228592. https://doi.org/10.1016/j.tecto.2020. 228592.

Dahl-Jensen, T., Larsen, T., Woelbern, I., Bach, T., Hanka, W., Kind, R., Gregersen, S., Mosegaard, K., Voss, P., Gudmundsson, A., 2003. Depth to Moho in Greenland: Receiver-function analysis suggests two Proterozoic blocks in Greenland. Earth Planet. Sci. Lett. 205, 379–393.

Data Management Centre of China National Seismic Network, 2007. Waveform data of China National Seismic Network. Institute of Geophysics, China Earthquake Administration. http://www.seisdmc.ac.cn. https://doi.org/10.11998/SeisDmc/SN.

Deng, Y.F., Zhang, Z., Fan, W., Perez-Gussinye, M., 2014. Multitaper spectral method to estimate the elastic thickness of South China: Implications for intracontinental deformation. Geosci. Front. 5, 193–203.

Dueker, K., Sheehan, A., 1997. Mantle discontinuity structure from midpoint stacks of converted P and S waves across the Yellowstone hotspot track. J. Geophys. Res. Solid Earth 102, 8313–8327. https://doi.org/10.1029/96JB03857.

Farra, V., Vinnik, L., 2000. Upper mantle stratification by P and S receiver functions. Geophys. J. Int. 141, 699–712.

Faure, M., Sun, Y., Shu, L., Monié, P., Charvet, J., 1996. Extensional tectonics within a subduction-type orogen. The case study of the Wugongshan dome (Jiangxi Province, southeastern China). Tectonophysics 263 (1–4), 77–106.

Faure, M., Shu, L., Wang, B., Charvet, J., Choulet, F., Monié, P., 2009. Intracontinental subduction: A possible mechanism for the Early Palaeozoic Orogen of SE China. Terra Nova 21 (5), 360–368.

Faure, M., Lin, W., Chu, Y., Lepvrier, C., 2016. Triassic tectonics of the southern margin of the South China Block. C. R. Geosci. 348, 5–14.

Faure, M., Chen, Y., Feng, Z., Shu, L., Xu, Z., 2017. Tectonics and geodynamics of South China: An introductory note. J. Asian Earth Sci. 141, 1–6.

Gao, S., Mihai, N., Jin, Z., Jason, B., 1998. Lower crustal delamination and evolution of continental crust. Geologi. J. China Univ. 4 (3), 241–249.

Hacker, B., Wallis, S., Ratschbacher, L., Grove, M., Gehrels, G., 2006. High- temperature geochronology constraints on the tectonic history and architecture of the ultrahigh-pressure Dabie-Sulu Orogen. Tectonics 25, TC5006. https://doi.org/10.1029/2005TC001937.

He, L., 2014. Numerical modeling of convective erosion and peridotite-melt interaction in big mantle wedge: Implications for the destruction of the North China Craton. J. Geophys. Res. Solid Earth 119 (4), 3662–3677. https://doi.org/10.1002/2013jb010657.

Jaupart, C., Mareschal, J.C., Iarotsky, L., 2016. Radiogenic heat production in the continental crust. Lithos 262, 398–427. https://doi.org/10.1016/j.lithos.2016.07.017.

Jiang, G., Hu, S., Shi, Y., Zhang, C., Wang, Z., Hu, D., 2019. Terrestrial heat flow of continental China: Updated dataset and tectonic implications. Tectonophysics 753, 36–48.

Kennett, B., Engdahl, E., 1991. Travel times for global earthquake location and phase identification. Geophys. J. Int. 105, 429–465.

Kind, R., Kosarev, G., Petersen, N., 1995. Receiver functions at the stations of the German Regional Seismic Network (GRSN). Geophys. J. Int. 121, 191–202.

Kosarev, G., Kind, R., Sobolev, S., Yuan, X., Hanka, W., Oreshin, S., 1999. Seismic evidence for a detached Indian lithospheric mantle beneath Tibet. Science 283, 1306–1309.

Kumar, P., Kind, R., Hanka, W., Wylegalla, K., Reigber, C., Yuan, X., Woelbern, I., Schwintzer, P., Fleming, K., Dahl-Jensen, T., Larsen, T., Schweitzer, J., Priestley, K., Gudmundsson, O., Wolf, D., 2005a. The Lithosphere-asthenosphere boundary in the North-West Atlantic region. Earth Planet. Sci. Lett. 236, 249–257.

Kumar, P., Yuan, X., Kind, R., Kosarev, G., 2005b. The lithosphere-asthenosphere boundary in the Tien Shan-Karakoram region from S receiver functions: Evidence for continental subduction. Geophys. Res. Lett. 32, L07305 https://doi.org/10.1029/2004GL022291.

Kumar, P., Yuan, X., Kind, R., Mechie, J., 2012. The lithosphere–asthenosphere boundary observed with USArray receiver functions. Solid Earth 3 (1), 149–159. https://doi.org/10.5194/se-3-149-2012.

Li, Z., Li, X., 2007. Formation of the 1300-km-wide intracontinental orogen and postorogenic magmatic province in Mesozoic South China: A flat-slab subduction model. Geology 35 (2), 179–182. https://doi.org/10.1130/G23193A.1.

Li, X., Li, W., Li, Z., Lo, C., Wang, J., Ye, M., Yang, Y., 2009. Amalgamation between the Yangtze and Cathaysia Blocks in South China: constraints from SHRIMP U-Pb zircon ages, geochemistry and Nd–Hf isotopes of the Shuangxiwu volcanic rocks. Precambr. Res. 174, 117–128.

Li, X., Li, Z., Li, W., Wang, X., Gao, Y., 2013b. Revisiting the "C-type adakites" of the Lower Yangtze River Belt, central Eastern China: In-situ zircon Hf-O isotope and geochemical constraints. Chem. Geol. 345, 1–15. https://doi.org/10.1016/j.chemgeo.2013.02.024.

Li, H., Song, X., Lü, Q., Yang, X., Deng, Y., Ouyang, L., Li, J., Li, X., Jiang, G., 2018. Seismic imaging of lithosphere structure and upper mantle deformation beneath east-central China and their tectonic implications. J. Geophys. Res. Solid Earth 123. https://doi.org/10.1002/2017JB014992.

Li, J., Zhang, Y., Dong, S., Su, J., Li, Y., Cui, J., Shi, W., 2013a. The Hengshan low-angle normal fault zone: structural and geochronological constraints on the late Mesozoic crustal extension in South China. Tectonophysics 606, 97–115.

Li, X., Zhu, P., Kusky, T., Gu, Y., Peng, S., Yuan, Y., Fu, J., 2015. Has the Yangtze craton lost its root? A comparison between the North China and Yangtze cratons. Tectonophysics 655, 1–14.

Liao, J., Wang, Q., Gerya, T., Ballmer, M., 2017. Modeling craton destruction by hydration-induced weakening of the upper mantle. J. Geophys. Res. Solid Earth 149 (1), 133. https://doi.org/10.1002/2017jb014157.

Ligorría, J., Ammon, C., 1999. Iterative deconvolution and receiver function estimation. Bull. Seismol. Soc. Am. 89 (5), 1395–1400.

Ling, M., Wang, F., Ding, X., Hu, Y., Zhou, J., Zartman, R., Yang, X., Sun, A., 2009. Cretaceous ridge subduction along the lower Yangtze River belt, Eastern China. Econ. Geol. 104 (2), 303–321. https://doi.org/10.2113/gsecongeo.104.2.303.

Liu, J., Cai, R., Pearson, D., Scott, J., 2019. Thinning and destruction of the lithospheric mantle root beneath the North China Craton: A review. Earth Sci. Rev. 196, 102873 https://doi.org/10.1016/j.earscirev.2019.05.017.

Liu, L., Klemperer, S. L., Blanchette, A. R. 2021. Western Gondwana imaged by S receiver-functions (SRF): New results on Moho, MLD (mid-lithospheric discontinuity) and LAB (lithosphere-asthenosphere boundary). Gondwana Res., 96, 206–218. 10.1016 /j.gr.2021.04.009.

Liu, L., Liu, L., Xu, Y., 2021a. Mesozoic intraplate tectonism of East Asia due to flat subduction of a composite terrane slab. Earth Sci. Rev. 214, 103505.

Liu, C., Wu, F., Sun, J., Chu, Z., Qiu, Z., 2012. The Xinchang peridotite xenoliths reveal mantle replacement and accretion in southeastern China. Lithos 150 (10), 171–187.

Lü, Q., Shi, D., Liu, Z., Zhang, R., Dong, S., Zhao, J., 2015. Crustal structure and geodynamics of the Middle and Lower reaches of Yangtze metallogenic belt and neighboring areas: Insights from deep seismic reflection profiling. J. Asian Earth Sci. 114, 704–716. https://doi.org/10.1016/j.jseaes.2015.03.022.

Mao, J., Xie, G., Duan, C., Pirajno, F., Ishiyama, D., Chen, Y., 2011. A tectono-genetic model for porphyry-skarn-stratabound Cu-Au-Mo-Fe and magnetite-apatite deposits along the Middle-Lower Yangtze River Valley, Eastern China. Ore Geol. Rev. 43 (1), 294–314. https://doi.org/10.1016/j.oregeorev.2011.07.010.

Meng, Q., Zhang, G., 2000. Geologic framework and tectonic evolution of the Qinling orogen, central China. Tectonophysics 323 (3–4), 183–196. https://doi.org/10.1016/S0040-1951(00) 00106-2.

Ouyang, L., Li, H., Lü, Q., Yang, Y., Li, X., Jiang, G., Zhang, G., Shi, D., Zheng, D., Sun, S., Tan, J., Zhou, M., 2014. Crustal and uppermost mantle velocity structure and its

relationship with the formation of ore districts in the Middle-Lower Yangtze River region. Earth Planet. Sci. Lett. 408, 378–389.
Pei, S., Zhao, J., Sun, Y., 2007. Upper mantle seismic velocities and anisotropy in China determined through Pn and Sn tomography. J. Geophys. Res. Solid Earth 112, B05312. https://doi.org/10.1029/2006JB004409.
Rychert, C., Rondenay, S., Fischer, K., 2007. P-to-S and S-to-P imaging of a sharp lithosphere –asthenosphere boundary beneath Eastern North America. J. Geophys. Res. Solid Earth 112 (B8). https://doi.org/10.1029/2006JB004619.
Shan, B., Afonso, J., Yang, Y., Grose, C., Zheng, Y., Xiong, X., Zhou, L., 2014. The thermochemical structure of the lithosphere and upper mantle beneath South China: Results from multiobservable probabilistic inversion. J. Geophys. Res. Solid Earth 119, 8417–8441.
Shan, B., Zhou, W., Xiao, Y., 2020. Lithospheric thermal and compositional structure of South China jointly inverted from multiple geophysical observations. Sci. China Earth Sci. 64, 148–160.
Shen, X., 2011. Study on the low-velocity discontinuity at the depth of 170 km beneath SSE station in Shanghai, China (in Chinese). Chin. J. Geophys 54, 698–705.
Shi, Y., Niu, F., Li, Z., Huangfu, P., 2020. Craton destruction links to the interaction between subduction and mid-lithospheric discontinuity: Implications for the eastern North China Craton. Gondwana Res. 83, 49–62. https://doi.org/10.1016/j.gr.2020.01.016.
Shu, L., Zhou, G., Shi, Y., Yin, J., 1994. Study of the high-pressure metamorphic blueschist and its Late Proterozoic age in the Eastern Jiangnan belt. Chin. Sci. Bull. 39, 1200–1204.
Shu, L., Faure, M., Jiang, S., Yang, Q., Wang, Y., 2006. SHRIMP zircon U-Pb age, litho and biostratigraphic analyses of the Huaiyu Domain in South China. Episodes 29, 244–252.
Sun, P., Guo, P., Niu, Y., 2021. Eastern China continental lithosphere thinning is a consequence of paleo-Pacific plate subduction: A review and new perspectives. Earth Sci. Rev. 218, 103680 https://doi.org/10.1016/j.earscirev.2021.103680.
Sun, W., Ling, M., Yang, X., Fan, W., Ding, X., Liang, H., 2010. Ridge subduction and porphyry copper-gold mineralization: An overview. Sci. China Earth Sci. 53 (4), 475–484. https://doi.org/10.1007/s11430-010-0024-0.
Sun, W., Yang, X., Fan, W., Wu, F., 2012. Mesozoic large-scale magmatism and mineralization in South China: Preface. Lithos 150 (5), 1–5.
VanDecar, J., Crossen, R., 1990. Determination of teleseismic relative phase velocity arrival times using multichannel cross-correlation and least squares. Bull. Seismol. Soc. Am. 80 (1), 150–169.
Vinnik, L., 1977. Detection of waves converted from P to SV in the mantle. Phys. Earth Planet. In. 15, 39–45.
Wang, Y., 2006. The onset of the Tan-Lu fault movement in Eastern China: Constraints from zircon (SHRIMP) and 40Ar/39Ar dating. Terra Nova 18 (6), 423–431. https://doi.org/10.1111/j.1365-3121.2006.00708.x.
Wang, Z., Kusky, T., Capitanio, F., 2018. On the role of lower crust and midlithosphere discontinuity for cratonic lithosphere delamination and recycling. Geophys. Res. Lett. 45 (15), 7425–7433. https://doi.org/10.1029/2017gl076948.
Wang, Q., Song, X., Ren, J., 2017. Ambient noise surface wave tomography of marginal seas in east Asia. Earth Planet. Phys. 1 (1), 13–25. https://doi.org/10.26464/epp2017003.
Wei, W., Chen, Y., Faure, M., Martelet, G., Lin, W., Wang, Q., Yan, Q., Hou, Q., 2016. An early extensional event of the South China Block during the Late Mesozoic recorded by the emplacement of the Late Jurassic syntectonic Hengshan Composite Granitic Massif (Hunan, SE China). Tectonophysics 672, 50–67. https://doi.org/10.1016/j.tecto.2016.01.028.
Wessel, P., Smith, W., 1995. New, improved version of generic mapping tools released. Eos Trans. 79, 47.
Wu, F., Ge, W., Sun, D., Guo, C., 2003a. Discussion on the lithosphere thinning in Eastern China. Earth Sci. Front. (China Univ. Geosci., Beijing) 10 (3), 51–60.
Wu, F., Walker, R., Ren, X., Sun, D., Zhou, X., 2003b. Osmium isotopic constraints on the age of lithospheric mantle beneath north Eastern China. Chem. Geol. 196 (1–4), 107–129. https://doi.org/10.1016/S0009-2541(02)00409-6.
Xiong, S., Yang, H., Ding, Y., Li, Z., 2016. Characteristics of Chinese continent Curie point isotherm. Chin. J. Geophys. 59 (10), 3604–3617. https://doi.org/10.6038/cjg20161008.
Xu, P., Liu, F., Wang, Q., Cong, B., Chen, H., 2001. Slab-like high velocity anomaly in the uppermost mantle beneath the Dabie-Sulu orogen. Geophys. Res. Lett. 28 (9), 1847–1850. https://doi.org/10.1029/2000GL012187.
Xu, J., Shinjo, R., Defant, M., Wang, Q., Rapp, R., 2002. Origin of Mesozoic adakitic intrusive rocks in the Ningzhen area of East China: Partial melting of delaminated lower continental crust? Geology 30 (12), 1111–1114.
Yin, A., 2010. Cenozoic tectonic evolution of Asia: A preliminary synthesis. Tectonophysics 488 (1–4), 293–325. https://doi.org/10.1016/j.tecto.2009.06.002.
Yu, H., Xu, Z., Cheng, R., Zhang, Z., Gao, D., 2023. Late Mesozoic transformation from the compressive to extensional tectonic regime of the Eastern North China Craton: sedimentary records from the North Yellow Sea Basin. J. Asian Earth Sci., 105809 https://doi.org/10.1016/j.jseaes.2023.105809.
Yuan, X., Kind, R., Li, X., Wang, R., 2006. The S receiver functions: synthetics and data example. Geophys. J. Int. 165 (2), 555–564. https://doi.org/10.1111/j.1365-246X.2006.02885.x.
Zhai, M., Santosh, M., 2011. The early Precambrian odyssey of North China craton: A synoptic overview. Gondwana Res. 20 (1), 6–25. https://doi.org/10.1016/j.gr.2011.02.005.
Zhang, Y., Chen, L., Ai, Y., Jiang, M., Xu, W., Shen, Z., 2018. Lithospheric structure of the South China Block from S-receiver function. Chin. J. Geophys. 61, 138–149.
Zhang, Y., Fang, H., Qiu, G., Ai, Y., Zhao, L., 2019. The lithospheric structure of the lower Yangtze Craton and its adjacent regions by S receiver function imaging. Geol. China 46 (4), 786–794.
Zhang, R., Liou, J., Ernst, W., 2009. The Dabie-Sulu continental collision zone: a comprehensive review. Gondwana Res. 16 (1), 1–26.
Zhao, L., Zheng, T., Chen, L., Tang, Q., 2007. Shear wave splitting in Eastern and central China: Implications for upper mantle deformation beneath continental margin. Phys. Earth Planet. In. 162 (1–2), 73–84. https://doi.org/10.1016/j.pepi.2007.03.004.
Zheng, Y., Fu, B., Gong, B., Li, L., 2003. Stable isotope geochemistry of ultrahigh pressure metamorphic rocks from the Dabie-Sulu orogen in China: Implications for geodynamics and fluid regime. Earth Sci. Rev. 62 (1–2), 105–161. https://doi.org/10.1016/S0012-8252(02)00133-2.
Zheng, Y., Xiao, W., Zhao, G., 2013. Introduction to tectonics of China. Gondwana Res. 23 (4), 1189–1206.
Zheng, X., Yao, Z., Liang, J., Zheng, J., 2010. The role played and opportunities provided by IGP DMC of China National Seismic Network in Wenchuan earthquake disaster relief and researches. Bull. Seismol. Soc. Am. 100 (5B), 2866–2872. https://doi.org/10.1785/0120090257.
Zheng, T., Zhao, L., He, Y., Zhu, R., 2014. Seismic imaging of crustal reworking and lithospheric modification in Eastern China. Geophys. J. Int. 196 (2), 656–670.
Zhou, X., Li, W., 2000. Origin of Late Mesozoic igneous rocks in south Eastern China: Implications for lithosphere subduction and underplating of mafic magmas. Tectonophysics 326 (3–4), 269–287. https://doi.org/10.1016/S0040-1951(00)00120-7.
Zhou, X., Sun, T., Shen, W., Shu, L., Niu, Y., 2006. Petrogenesis of Mesozoic granitoids and volcanic rocks in South China: A response to tectonic evolution. Episodes 29 (1), 26–33.
Zhou, L., Xie, J., Shen, W., Zheng, Y., Yang, Y., Shi, H., Ritzwoller, M., 2012. The structure of the crust and uppermost mantle beneath South China from ambient noise and earthquake tomography. Geophys. J. Int. 189 (3), 1565–1583.
Zhu, L., 2000. Crustal structure across the San Andreas Fault, southern California from teleseismic converted waves. Earth Planet. Sci. Lett. 179, 183–190.
Zhu, L., 2002. Deformation in the lower crust and downward extent of the San Andreas Fault as revealed by teleseismic waveforms. Earth Planets Space 54, 1005–1010.
Zhu, L., Kanamori, H., 2000. Moho depth variation in southern California from teleseismic receiver functions. J. Geophys. Res. Solid Earth 105, 2969–2980.
Zhu, R., Xu, Y., Zhu, G., Zhang, H., Zheng, T., 2012a. Destruction of the North China Craton. Sci. China Earth Sci. 55 (10), 1565–1587.
Zhu, R., Yang, J., Wu, F., 2012b. Lithos timing of destruction of the North China craton. Lithos 149, 51–60.